

# CFD simulation of wind-driven upward cross ventilation and its enhancement in long buildings: Impact of single-span versus double-span leeward sawtooth roof and opening ratio

J. I. Perén<sup>a,b,1</sup>, T. van Hooff<sup>c</sup>, B.C.C. Leite<sup>a</sup>, B. Blocken<sup>b,c</sup>

<sup>a</sup> Civil Construction Engineering Department, Polytechnic School of the University of São Paulo - USP, São Paulo, Brazil.

<sup>b</sup> Building Physics and Services, Eindhoven University of Technology, Eindhoven, The Netherlands.

<sup>c</sup> Building Physics Section, Leuven University, Leuven, Belgium.

## Abstract

A leeward sawtooth roof building has an inlet opening in the lower level of the windward facade and an upper-level outlet opening near the roof top, in the leeward facade. Leeward sawtooth roof buildings can be applied to efficiently ventilate low-rise buildings. Previous studies of the authors showed that the ventilation potential strongly depends on the roof inclination angle and roof geometry. The current study focuses on the ventilation flow in single-zone elongated low-rise buildings with a single-span versus double-span leeward sawtooth roof and different opening ratios. Straight, concave and convex roof geometries are evaluated. The analysis is performed using 3D steady Reynolds-averaged Navier-Stokes Computational Fluid Dynamics (CFD) simulations with the SST  $k-\omega$  turbulence model. The computational grid is based on a grid-sensitivity analysis and the simulation results are validated based on Particle Image Velocimetry (PIV) measurements from literature. For the single-span cases, the convex roof results in the highest volume flow rate, which is about 8.8% higher than for the concave roof, and 3.5% higher than the straight roof. A double-span roof performs slightly better than a single-span roof with respect to ventilation flow rates (below 4.2%) in case of a straight or concave roof, but worse in case of a convex roof (-12%). The internal roof geometry near the outlet opening plays an important role in the ventilation of the building. Finally, the inlet-to-outlet opening ratio has an important effect on the volume flow rates, with significantly higher ventilation flow rates for a lower opening ratio.

*Keywords: Computational Fluid Dynamics (CFD), Urban physics, Natural ventilation, Leeward sawtooth roof geometry, Upward cross-ventilation, Double-span leeward sawtooth roof building.*

## Highlights

- CFD simulations of natural cross-ventilation flow with 3D steady RANS.
- Grid-sensitivity analysis and validation with PIV measurements.
- Influence of single and double-span leeward sawtooth roof geometry on flow rate and indoor velocities.
- Highest volume flow rates with convex roof geometries.
- Size and magnitude of underpressure zone in the wake mainly depend of the first-span geometry.

---

<sup>1</sup> Corresponding author: E-mail address: [j.i.peren.montero@tue.nl](mailto:j.i.peren.montero@tue.nl). Tel.: +31 (0) 40 247 3667  
Fax +31 (0)40 243 8595. PO Box 513, 5600 MB, Eindhoven.

## 1 Introduction

Elongated naturally-ventilated buildings are used in a wide range of applications, such as hospitals, schools, industrial facilities, commercial buildings and even residential buildings. However, in elongated naturally-ventilated buildings, the cross-ventilation efficiency can become problematic as the ventilation rate generally decreases with the building length [1]. Long low-rise buildings with a flat roof require a significant increase of the pressure differences over the building to overcome the higher indoor resistance due to the larger distance between the inlet and outlet opening. However, buildings with side-wall and roof openings can increase the ventilation flow rate [2,3] and can therefore be an option for the ventilation of elongated buildings. For instance, a leeward sawtooth roof building, with inlet openings at the lower part of the windward facade and outlet openings at roof level, might still achieve enough efficient cross-ventilation in elongated buildings. Furthermore, compared to elongated buildings with a flat roof, buildings with a leeward sawtooth roof can achieve more uniform and higher daylight intensity levels due to the openings in the roof construction [4].

In the last decades, several studies have been conducted on wind-induced loads on low-rise buildings [5-14]. These studies involved different roof geometries; i.e. gable roofs [7-9], arched roofs [10], mono-sloped roofs or shed roofs [11,12], other roof geometries [13,14] and multi-span roofs including multi-span sawtooth roofs [5,6,12]. In addition, some studies were performed of wind-driven cross-ventilation in low-rise buildings with a pitched roof and asymmetric openings [2,3,15-29] as is studied in this paper. Gandemer and Barnaud [24], and Perén et al. [26-28] carried out studies on mono-sloped or shed roofs (single-span sawtooth roof) and their findings support the understanding of airflow inside and around a complex building such as a multi-span sawtooth roof building. For instance, Gandemer and Barnaud [24] indicated the importance of the orientation by pointing out the advantage of a leeward orientation of the sawtooth roof compared to a windward orientation in wind-driven cross-ventilation of sawtooth roof or shed-roof buildings. Previous studies by the authors showed that the volume flow rate depends – among others – on the roof inclination angle [26], the roof geometry [27] and the eaves configuration [28]. Concerning multi-span roof buildings, such as sawtooth roof buildings, some studies focused on the ventilation performance of greenhouses (e.g. [2,3,15-22,29]). For example, Fatnassi et al. [22] provided information on how to optimize the ventilation rates using the building orientation. Bournet et al. [29] provided a review on the effect of ventilation opening configuration on the indoor climate of greenhouses and highlighted that the analysis of the response of a greenhouse to outdoor climatic conditions will help to better adjust ventilation management and to develop a more efficient ventilation design. However, so far, guidelines extracted from systematic studies for multi-span buildings are rare. Therefore, the aim of the current study is to compare the performance of single-span and double-span leeward sawtooth roof configurations and to evaluate the effect of the opening ratio in an elongated long building. The ventilation performance evaluation is based on the volume flow rate through the building and the indoor air velocity in the occupied zone [30], considering that the ventilation rate is not always the best criterion for evaluating the performance of ventilation systems [3].

In the current paper, a coupled Computational Fluid Dynamics (CFD) approach (e.g. [19,23,31-37]) is employed using the 3D steady Reynolds-Averaged Navier–Stokes (RANS) equations. The coupled approach enables a detailed analysis of the indoor and outdoor airflow by conducting one CFD simulation in which the indoor and outdoor airflow are modeled simultaneously and within the same computational domain. Section 2 presents the building geometries that are studied. The validation study using Particle Image Velocimetry (PIV) measurements of upward cross-ventilation from literature is presented in Section 3, after which the CFD model for the case study is outlined in Section 4. The results are presented in Section 5 and Section 6. Discussion (Section 7) and conclusions (Section 8) conclude this paper.

## 2 Building geometries

Figure 1 is a schematic representation of the three groups of different roof geometries selected for this study:

- three single-span cases (Fig. 1a), with inlet-to-outlet opening ratio ( $OR = A_{inlet}/A_{outlet,total} = 1$ , with  $A_{outlet,total}$  the sum of the two outlet openings areas) (same area for both openings);
- three double-span cases (Fig. 1b) with the same inlet-to-outlet opening ratio ( $OR = 1$ ). The outlet openings have the same width but only half the height as the inlet opening;

- three cases with the same double-span roof but with a lower opening ratio (OR = 0.5) (Fig. 1c). The two outlet openings have the same width and height as the inlet opening;

The three different roof geometries are designated by a letter: A, B, and E, to refer to their base cases. These numbers originate from a previous study of the authors [27] focused on cross-ventilation of single-span buildings with a depth of 6 m, as opposed to 12 m in the present study. Geometry A has a straight roof, geometry B has a concave roof, and geometry E has a convex roof. Note that we adopt the definitions of “convex” and “concave” as used in the description of mathematical functions, where “a convex function is a continuous function whose value at the midpoint of every interval in its domain does not exceed the arithmetic mean of its values at the ends of the interval” [38]. For all cases, the number “2” after a letter (i.e., A2, B2, and E2) indicates that the depth of this geometry is two times the depth (D) of its base case in [6]. Since the base case has a horizontal plan area of  $3 \times 6 \text{ m}^2$  (W x D), the cases studied in this paper have a more elongated horizontal plan area of  $3 \times 12 \text{ m}^2$  (W x D). The double-span cases have two roofs (double span) and two outlet openings (one in each part of the double-span roof) instead of one and are therefore indicated with “x2” (i.e., A2x2, B2x2 and E2x2). The description “OR” stands for “opening ratio” and the subsequent number provides this ratio, i.e. 1 for the case with total outlet opening area equal to the inlet opening area and 0.5 for the case with total outlet opening area equal to two times the size of the inlet opening area. Note that Karava et al. [39] stated that higher volume flow rates can be achieved when the opening ratio is smaller than 1 ( $A_{\text{inlet}}/A_{\text{outlet}} < 1$ ). The implicit roof inclination angle, which is the angle of a line from the upwind roof edge till the top roof edge, is  $18^\circ$  for all the single-span cases, and  $27^\circ$  for each span of the double-span cases. Note that the base cases (i.e., A, B, E) previously studied in [27] also have an implicit roof inclination angle of  $27^\circ$ .

Figure 2 shows a front view (Fig. 2a), a vertical cross-section (Fig. 2b) and a perspective view (Fig. 2c) of the building with roof geometry E2 with its main dimensions. All studied geometries have the same: (a) maximum roof height ( $H = 5.7 \text{ m}$ ); (b) building depth ( $D = 12 \text{ m}$ ), (c) building width ( $W = 3 \text{ m}$ ); (d) inlet opening size (corresponding to 5% windward wall porosity); and (e) inlet and outlet opening location (the outlet is located at  $\frac{3}{4} D$ ). Since all three buildings have different roof geometries, they all have different internal volumes, which are listed in Table 1. The building width is taken equal to 3 m as this width can be considered as the minimum distance in a building with a corridor. Furthermore, a building width of 3 m is equal to the width of the buildings that were studied in previous publications by the authors [26-28], and thus facilitates a comparison between all these geometries. The distances from the ground to the bottom of the inlet and outlet opening are 1.42 m and 4.60 m, respectively. Note that the upper edges of the outlet openings on the leeward wall are not flat, while the lower edges are flat. This is due to the fact that in a previous paper by the authors [27], a concave roof geometry (E) was studied of which the specific interior geometry did not allow for flat upper edges of the outlet openings. In order to keep the same window geometry for all cases studied in this broader research project, it was decided to use this specific opening geometry for all cases, including the ones reported in this paper.

### 3 CFD simulations: validation study

Validation is obligatory to determine the accuracy and reliability of the results of CFD simulations based on the 3D steady RANS equations [40-42]. A general overview of the validation study will be provided in this section, a more detailed description of the simulations and an elaborate discussion on the results can be found in another recent publication by the authors [26]. Note that a validation study based on velocities is performed since the coupled approach is employed for this study, i.e. the outdoor wind flow and indoor airflow are modeled simultaneously and within the same computational domain. In addition, the focus in this study is mainly on the velocities and the volume flow rates through the building, and the latter is calculated by taking the surface integral of the velocity at the inlet opening. If the focus would be mainly on the pressure field around and inside the building, a validation study using pressure measurements might be considered as a good option as well, as for example reported by Shen et al. [25].

### 3.1 Wind-tunnel experiment

Karava et al. performed reduced-scale PIV wind-tunnel measurements of wind-induced cross-ventilation in a generic isolated building geometry [39]. The measurement results for the asymmetric location of the openings (upward cross-ventilation) are used for model validation in the present study. The dimensions of the reduced-scale building model (1:200) are  $0.1 \times 0.1 \times 0.08 \text{ m}^3$  (W x D x H), as shown in Figure 3a and 3b. This corresponds to full-scale dimensions  $20 \times 20 \times 16 \text{ m}^3$  (W x D x H). The openings have a fixed height of 0.018 m (3.6 m full scale) and for this validation study, the building model with an inlet opening at the bottom of the windward facade (center of the opening at  $h = 0.02 \text{ m}$ ) and an outlet opening at the top of the opposite (leeward) facade (center of the opening at  $h = 0.06 \text{ m}$ ) and a wall porosity of 10% is selected. The reduced-scale aerodynamic roughness length in the wind-tunnel measurements was  $z_0 = 0.025 \text{ mm}$ , which corresponds to 0.005 m in full scale [20]. The reference mean wind speed at building height ( $z_{\text{ref}} = H$ ) was  $U_{\text{ref}} = 6.97 \text{ m/s}$  and the reference turbulence intensity at building height was 10%. The turbulence intensity was about 17% near ground level (0.012 m) and 5% at gradient height (0.738 m). For more information related to the wind-tunnel experiments the reader is referred to [39,43].

### 3.2 CFD settings and parameters

The computational model represents the reduced-scale model used in the experiments and follows the best practice guidelines by Franke et al. [40], Tominaga et al. [41] and Blocken [42]. However, the upstream length of the domain is reduced to 3 times the height of the building to limit the development of unintended streamwise gradients [44,45]. The dimensions of the domain are  $0.9 \times 1.54 \times 0.48 \text{ m}^3$  (W x D x H) at reduced-scale (1:200). The computational grid is created using the surface-grid extrusion technique by van Hooff and Blocken [23] and is shown in Figure 3c and 3d (vertical cross-section and perspective view). The grid resolution resulted from a grid-sensitivity analysis yielding a fully structured hexahedral grid with 770,540 cells. At the inlet of the domain the vertical approach-flow profiles (log-law mean wind speed  $U$ , turbulent kinetic energy  $k$  and specific dissipation rate  $\omega$ ) are imposed, based on the measured incident profiles of mean wind speed  $U$  and longitudinal turbulence intensity  $I_U$  of the experiment. More information on the boundary conditions can be found in Ref. [26]. The commercial CFD code ANSYS Fluent 12 is used to perform the simulations [46]. The 3D steady RANS equations are solved in combination with the Shear-Stress Transport  $k-\omega$  model (SST  $k-\omega$ ) [47]. The SST  $k-\omega$  model was selected after a detailed validation study [26] including an analysis of six commonly employed RANS turbulence models: (1) the standard  $k-\epsilon$  model [48]; (2) the realizable  $k-\epsilon$  model [49]; (3) the renormalization group (RNG)  $k-\epsilon$  model [50,51]; (4) the standard  $k-\omega$  model [52]; (5) the Shear-Stress Transport  $k-\omega$  model (SST  $k-\omega$ ) [47]; and (6) a Reynolds Stress Model (RSM) [53]. From this comparison it became clear that the SST  $k-\omega$  model and the RNG  $k-\epsilon$  model provided the best agreement with the PIV measurements from literature [39], with a slightly better performance of the SST  $k-\omega$  model [26]. The same conclusion was drawn in a previous validation study by Ramponi and Blocken [32] for cross-ventilation flow in a generic building with symmetric ventilation openings. The SIMPLE algorithm is used for pressure-velocity coupling, pressure interpolation is second order and second-order discretization schemes are used for both the convection terms and the viscous terms of the governing equations.

### 3.3 Comparison between CFD simulations and wind tunnel-measurements

Figure 4a and 4b display the mean velocity vector field in the vertical center plane obtained from PIV measurements and CFD simulations, respectively. It is observed that the CFD simulations correctly predict the most important flow features: the standing vortex upstream of the building and the specific flow pattern inside the building, which exhibits a strong downward directed flow near the inlet opening followed by a strong upwards directed flow along the downstream wall, which leads to an oblique upward directed flow through the outlet opening. To provide a more quantitative comparison the measured and computed streamwise wind speed ratios  $U/U_{\text{ref}}$  along (1) a horizontal line going through the middle of the windward opening (Fig. 4c), and (2) along a diagonal line (Fig. 4d), are presented [26]. The comparison indicates a good agreement between the measurement data and the results from the CFD simulations using the SST  $k-\omega$  turbulence model to provide

closure. It can be noticed that the simulations overestimate the mean velocity around the opening, which was also pointed out by Ramponi and Blocken [32] in their study of cross-ventilation with symmetric window openings (both openings at same height). This discrepancy can be explained by the fact that the PIV measurements cannot provide accurate predictions in these regions due to reflections and shading effects [39]. Despite these differences an overall good agreement is observed.

Note that the geometry of the building in the wind-tunnel measurements by Karava et al. [39] (Fig. 3) and that of the single-span and double-span buildings as presented in the current paper (Fig. 1) are not identical, but there is a sufficient degree of similarity to consider this validation approach applicable for the leeward sawtooth roof buildings, for the following reasons: (1) both buildings are isolated, (2) both buildings consist of one internal zone, (3) asymmetric openings are present in both buildings (lower one in the windward and upper one in the leeward facade) and (4) both are exposed to a wind direction normal to the facade with the opening in the lower part of the facade. As a result, the salient flow features for the building studied by Karava et al. [39] are also present for the buildings studied in the present paper.

#### 4 CFD simulations of single and double-span roof geometries: settings and parameters

In this section the computational geometry, domain and grid, boundary conditions and solver settings for the evaluation of the single-span and double-span roofs are presented.

##### 4.1 Computational geometry, domain and grid

The computational model of the leeward sawtooth roof geometry E2 has dimensions as indicated in Section 2 and Figure 2. The computational domain is depicted in Figure 5a and is in accordance with the best practice guidelines as published by Franke et al. [40] and Tominaga et al. [41]. As in the validation study, the upstream length of the domain is reduced to 3 times the height of the building to limit horizontal inhomogeneity of the approach-flow profiles [44,45]. The surface-grid extrusion technique [23] is applied to construct the computational grid, which allows full control over the quality (size, shape) of every grid cell. The grid resolution is based on the grid-sensitivity analysis presented in Peren et al. [27]. The grid for case E2 is shown in Figure 5b-d. The total number of cells is 2,917,152 for case E2 and it varies for each of the cases with different roof geometries, ranging from 2.8 to 3.6 million cells.

##### 4.2 Boundary conditions

At the inlet of the domain the vertical approach-flow profiles of the mean wind speed  $U$ , turbulent kinetic energy  $k$  and specific dissipation rate  $\omega$  are imposed. The wind direction is perpendicular to the windward building facade. The inlet mean wind-velocity profile  $U(z)$  is defined according to the logarithmic law (Eq. 1):

$$U(z) = \frac{u_{ABL}^*}{\kappa} \ln\left(\frac{z + z_0}{z_0}\right) \quad (1)$$

with  $z_0 = 0.1$  m,  $u_{ABL}^*$  the atmospheric boundary layer (ABL) friction velocity,  $\kappa$  the von Karman constant (0.42) and  $z$  the height coordinate. The value of  $u_{ABL}^*$  is determined based on the values of the reference velocity ( $U_{ref} = 12.48$  m/s) at building height ( $z_{ref} = H = 5.7$  m), yielding a building Reynolds number of about 500,000. The aerodynamic roughness length is set higher than the one used in the validation study, to impose a more realistic wind velocity profile, corresponding to “roughly open country” [54]. The turbulent kinetic energy  $k(z)$  is calculated from the mean wind speed  $U(z)$  and the streamwise turbulence intensity  $I_u(z)$ , with a value of 15% at the top of the building model (at  $z_{ref} = H$ ) and 45% at ground level, using Eq. (2):

$$k(z) = a(I_u(z)U(z))^2 \quad (2)$$

with “a” a parameter ranging from 0.5 to 1.5 [18,27]. In the current work the value  $a = 0.5$  is used as in the

validation study and in previous studies by the authors [26-28], assuming that the turbulent fluctuations in the streamwise direction are much larger than those in lateral and vertical direction ( $\sigma_u \gg \sigma_v$  and  $\sigma_u \gg \sigma_w$ ). The specific dissipation rate  $\omega$  is given by Eq. (3), where  $C_\mu$  is an empirical constant taken equal to 0.09, and the turbulence dissipation rate  $\varepsilon$  is given by Eq. (4).

$$\omega(z) = \frac{\varepsilon(z)}{C_\mu k(z)} \quad (3)$$

$$\varepsilon(z) = \frac{u_{ABL}^{*3}}{\kappa(z + z_0)} \quad (4)$$

The SST k- $\omega$  model uses an automated wall treatment [46] for the ground and building surfaces, which automatically switches between (1) low-Reynolds number modeling; and (2) standard wall functions by Launder and Spalding [55] in conjunction with the sand-grain based roughness ( $k_s$ ) modification defined by Cebeci and Bradshaw [56]; depending on the mesh resolution near the wall. For the ground surfaces, the values of the roughness parameters, i.e. the sand-grain roughness height ( $k_s = 0.14$  m) and the roughness constant ( $C_s = 7$ ), are determined based on the relationship with the aerodynamic roughness length  $z_0$  derived by Blocken et al. [44]:

$$k_s = \frac{9.793z_0}{C_s} \quad (5)$$

The sand-grain roughness height is set to zero ( $k_s = 0$  m) for the building surfaces (smooth walls). At the outlet plane, zero static gauge pressure is applied and at the top and lateral sides of the domain zero normal velocities and zero normal gradients of all variables are imposed.

#### 4.3 Solver settings

The CFD simulations are performed using the commercial CFD code ANSYS Fluent 12 [46]. The 3D steady RANS equations are solved in combination with the SST k- $\omega$  turbulence model by Menter [47]. Pressure-velocity coupling is taken care of by the SIMPLE algorithm, pressure interpolation is second order and second-order discretization schemes are used for both the convection terms and the viscous terms of the governing equations. Convergence is assumed to be obtained when all the scaled residuals level off and reach a minimum of  $10^{-6}$  for x, y momentum,  $10^{-5}$  for y momentum and  $10^{-4}$  for k,  $\omega$  and continuity. After convergence is obtained, the error in mass flow balance of the indoor space is less than  $10^{-5}$ - $10^{-7}$ , depending on the case. As also observed by Ramponi and Blocken [32], the simulations show oscillatory convergence. To obtain a reliable steady value of the solution variables, the results are monitored over 10,400 iterations and the final values are obtained by averaging over 400 iterations (10,000-10,400), after the simulation reached a statistically stationary solution. The volume flow rate through the inlet opening is computed by averaging the product of the window opening area ( $m^2$ ) and the average velocity at the opening (m/s) during 400 iterations. More information on how to deal with oscillatory convergence can be found in Ref. [42].

## 5 CFD simulations of single and double-span roof geometries: results

Section 5.1 presents the performance of the three single-span leeward sawtooth roof geometries (OR = 1). Subsequently, Section 5.2 presents the results of the two cases of three double-span roof geometries (OR = 1 and OR = 0.5). The ventilation performance of all leeward sawtooth roof geometries (single-span and double-span) is assessed based on the volume flow rate through the building. In addition, the airflow pattern around and inside the building is analyzed for all cases. Finally, for the cases with a convex roof geometry (E), the non-dimensional velocity magnitude ( $|V|/U_{ref}$ ) along four horizontal lines at four different heights (h) from the ground floor; i.e. h = 0.1 m, 0.6 m, 1.1 m, and 1.7 m, is presented.

### 5.1 Single-span leeward sawtooth roof geometries

Figure 6a shows the volume flow rates in percentage (%) for the single-span roof geometries, in which the convex geometry E2 reaches the highest volume flow rate ( $= 3.04 \text{ m}^3/\text{s}$ ) and is taken as the reference case ( $= 100\%$ ). The building with straight roof (A2) and concave roof (B2) reach values of 96.5% and 91.2%, respectively, of the volume flow rate compared to case E2. These results are consistent with previous results for similar buildings but with length  $L = 6 \text{ m}$  and an implicit roof inclination angle of  $27^\circ$  [27]. In addition, Figure 6b shows the area-averaged pressure coefficient  $C_p$  at the inlet and the outlet opening. The pressure coefficient is calculated as:

$$C_p = \frac{(P - P_0)}{(0.5\rho U_{ref}^2)} \quad (6)$$

where  $P$  is the static pressure,  $P_0$  the reference static pressure,  $\rho$  the density of air ( $= 1.225 \text{ kg/m}^3$ : International Standard Atmosphere (ISA); dry air,  $\theta_a = 15^\circ\text{C}$ ,  $p_0 = 101,325 \text{ Pa}$  [57]) and  $U_{ref}$  is the approach-flow wind speed at building height ( $U_{ref} = 12.48 \text{ m/s}$  at  $z_{ref} = 5.7 \text{ m}$ , yielding a building Reynolds number of about  $5 \times 10^5$ ). It can be seen that the values at the inlet are about equal (between 0.37 and 0.4). The value of  $C_p$  at the outlet is slightly higher for geometry E2 ( $C_p = -0.28$ ) than for the other two geometries, which indeed results in a slightly higher volume flow rate through the building. This is also consistent with the results from the previous study on less elongated buildings [27]. An overview of the  $C_p$  values at the inlet and outlet openings is provided in Table 2 as well.

In order to better analyze the effect of the roof geometry on the flow pattern around and inside the building, contours of  $C_p$  and of the non-dimensional velocity magnitude ( $|V|/U_{ref}$ ) in the vertical center plane are shown in Figure 7. The figures show that the pressure distribution upstream of the windward facade is almost identical for all three cases. However, they also show that the convex roof geometry E2 increases the size (height) and magnitude of the underpressure behind the building (wake region), resulting in a higher absolute value of the area-averaged  $C_p$  value in the outlet opening ( $C_p = -0.28$ ), compared to geometry B2 (Fig. 7c:  $C_p = -0.24$ ) and geometry A2 (Fig. 7a:  $C_p = -0.25$ ). The average internal pressure coefficients  $C_p$  for the three single-span cases are for geometry A2:  $C_p = 0.170$ ; for geometry B2:  $C_p = 0.215$ ; and for geometry E2:  $C_p = 0.185$ . Note that geometry B2, in contrast to geometry A2 and E2, has no flow separation at the windward roof edge (Fig. 7d) and the shear layer downstream of the roof end has a downward direction. As a consequence of the lower absolute value of the underpressure at the outlet opening and the higher internal pressure, the volume flow rate of the concave roof geometry B2 is 8.8% lower than that of the convex roof geometry E2, as previously shown in Figure 6. This is in line with the findings of the authors for a single-span roof with a depth of 6 m [27], which highlighted that convex roof geometries reach higher volume flow rates than concave roof geometries. Note that the geometries in the present study have an inclination angle of  $18^\circ$ , which is lower than in the previous study, where it was  $27^\circ$ .

### 5.2 Double-span leeward sawtooth roof geometries

The performance of double-span leeward sawtooth roof geometries is analyzed systematically by comparison with the corresponding single-span cases (i.e., straight, concave and convex). For all geometries, the corresponding single-span roof geometry is selected as the reference case. Table 2 provides an overview of the pressure coefficients at the inlet and outlet openings for all double-span leeward sawtooth roof geometries, and for the single-span roof geometries. A detailed analysis is provided in the following subsections.

#### 5.2.1. Straight roof geometry

Figure 8a displays the volume flow rates for the straight roof geometry cases (A2 – reference case –, A2x2\_OR1 and A2x2\_OR0.5) and shows that the double-span leeward roof with an opening ratio of 1 (A2x2\_OR1) reaches a slightly higher volume flow rate (increase of 1.4%) than the single-span reference case (A2). The case A2x2\_OR0.5 however reaches a 25.6% higher volume flow rate than A2. This increase of volume flow rate with

decreasing opening ratio (larger outlet openings) was already reported by Karava et al. [39] and can be attributed to the lower overall flow resistance as a result of the larger outlet opening (window opening area), which leads to more pressure equalization between the indoor and outdoor environment near the outlet. The increase is in line with what would expect based on the orifice equation for cross-ventilation flow. If one would assume (hypothetical situation) that the two leeward openings are actually one opening, then Eq. (7) can be used to calculate the wind-driven ventilation flow through two openings that are in series, based on the pressure coefficients on the windward ( $C_{P,W}$ ) and leeward facade ( $C_{P,L}$ ), the total discharge coefficient  $C_{D,total}$  and the equivalent window opening area  $A$ .

$$Q = C_{D,total} A U_{ref} \sqrt{C_{P,W} - C_{P,L}} \quad (7)$$

In which  $C_{D,total}A$  can be calculated using Eq. (8) (e.g. [39]).

$$C_{D,total}A = \frac{(C_{D1}A_1)(C_{D2}A_2)}{\sqrt{(C_{D1}A_1)^2 + (C_{D2}A_2)^2}} \quad (8)$$

With  $C_{D1}$  and  $C_{D2}$  the discharge coefficients of the inlet opening and outlet opening, respectively, and  $A_1$  the inlet opening area and  $A_2$  the outlet opening area. Based on Eq. (8) it can be deduced that a doubling of either the inlet or outlet opening area ( $A_1$  or  $A_2$ ) will lead to an increase of  $C_{D,total}A$  from  $1/\sqrt{2}$  to  $2/\sqrt{5}$ , i.e. with 26%, and thus in a theoretical increase of the flow rate with 26% if the surface pressures at the openings would remain the same. Only doubling of both opening area  $A_1$  and  $A_2$  would potentially double the volume flow rate for this hypothetical situation.

The contours of the  $C_p$  and  $|V|/U_{ref}$  are displayed in Figure 9. The figures show that the pressure distribution upstream of the windward facade is almost identical for the three cases. However, from Table 2 it can be seen that the local value of  $C_p$  at the inlet opening for A2x2\_OR0.5 ( $C_p = 0.25$ ) is lower than those obtained for A2 ( $C_p = 0.38$ ) and A2x2\_OR1 ( $C_p = 0.37$ ). In addition, they also show that double-span leeward sawtooth roofs (A2x2\_OR1 and OR0.5) strongly increase the absolute value of the underpressure zone behind the first span compared to the reference case A2. Furthermore, the absolute value of the underpressure behind the second span is a bit lower than that behind the single span of the reference case A2 (Table 2). Figure 9 also clearly shows a lower internal positive pressure in Figure 9e for A2x2\_OR0.5 ( $-0.10 < C_p < 0.03$ ), compared to A2x2\_OR1 ( $0.12 < C_p < 0.22$ ), which can be attributed to the higher pressure equalization resulting from the larger outlet openings for case A2x2\_OR0.5. This reduction in internal pressure increases the velocity of the jet entering the building and the resulting volume flow rate. This also explains why the volume flow rate for A2x2\_OR0.5 is higher than for A2x2\_OR1 albeit the lower pressure difference over the building openings. Figure 9f also shows that the inlet jet shifts to a slightly more horizontal direction. Note that the average internal pressure for the double-span geometry A2x2\_OR1 is about equal to the single-span geometry A2; i.e.  $C_p \approx 0.17$ , and therefore the volume flow rates of those geometries do not differ that much.

### 5.2.2. Concave roof geometry

Figure 8b displays the volume flow rates for the concave roof geometries (B2 – reference case –, B2x2\_OR1 and B2x2\_OR0.5) and shows that the volume flow rates for the double-span cases B2x2\_OR1 and B2x2\_OR0.5 increase with 4.2% and 28.0% compared to case B2, respectively. Contours of  $C_p$  and  $|V|/U_{ref}$  are given in Figure 10. It can be seen that the flow remains attached to the top of the first-span roof and that it also reattaches to the top of the second-span roof (Fig. 10d and f). The internal pressure in the building is lower in case B2x2\_OR0.5 ( $-0.02 < C_p < 0.08$ ) than in case B2 ( $0.17 < C_p < 0.25$ ) and B2x2\_OR1 ( $0.16 < C_p < 0.24$ ). In Table 2 it can be seen that also for the concave roof geometry the pressure at the inlet opening is lower for B2x2\_OR0.5 ( $C_p = 0.29$ ) than for B2x2\_OR1 ( $C_p = 0.4$ ), with pressures at the outlet openings that are about equal. However, due to the lower internal pressure the inlet jet velocity considerably increases in case B2x2\_OR0.5 (Fig. 10f) and leads to a higher volume flow rate through the building. The average internal pressure coefficient for B2x2\_OR1 ( $C_p = 0.20$ ) only slightly deviates from the value for the single-span geometry B2 ( $C_p = 0.215$ ) and therefore the volume flow rates of those two geometries do not differ that much.

### 5.2.3. Convex roof geometry

Concerning the convex roof geometries, it is the double-span roof geometry E2x2\_OR1 that results in the lowest volume flow rate, i.e. only 88.0% of the volume flow rate of the reference case E2 (see Figure 8c). This is in contrast to the previous roof geometry types, where the straight and concave double-span geometries reach slightly higher volume flow rates than the corresponding single-span geometry with the same opening ratio (i.e. 1.4% for A2x2\_OR1 (Fig. 9a) and 4.2% for B2x2\_OR1 (Fig. 9b)). The fact that case E2x2\_OR1 reaches a lower volume flow rate than E2 is probably due to the relatively narrow internal area on the inside of the outlet openings (see dashed circles in Fig. 11c) which appears to act as a resistance to the airflow near the outlet openings. As a result of this “blockage”, the internal  $C_p$  of case E2x2\_OR1 reaches slightly higher values than for the other two double-span cases with identical opening ratios; the internal  $C_p$  values for case E2x2\_OR1 range between 0.21 and 0.28 (Fig. 11c), with an average  $C_p$  value of 0.25, while for case A2x2\_OR1 they range between 0.12 and 0.22 (Fig. 9c) with an average  $C_p$  value of 0.17; and for case B2x2\_OR1 they range between 0.16 and 0.24 (Fig. 10c), with an average  $C_p$  value of 0.20. Note that only for the convex double-span roof geometry (E2x2\_OR1) the average internal pressure coefficient increases compared to the single-span geometry (E2); the increase in average internal pressure coefficient amounts 32% (from  $C_p = 0.19$  to  $C_p = 0.25$ ). The incoming airflow rate is reduced due to this higher internal pressure. However, E2x2\_OR1 reaches an underpressure at the outlet opening in the first span which is 64% higher (in absolute value) than that of case B2x2\_OR1. But this higher underpressure cannot compensate for the higher internal pressure. A wider internal outlet-opening geometry or a larger outlet opening area (lower OR) could maybe take advantage of the higher underpressure and could maybe result in a more efficient air exhaust. Indeed, for case E2x2\_OR0.5, although the  $C_p$  values at the inlet are lower for E2x2\_OR0.5 ( $C_p = 0.25$ ) than those in case E2x2\_OR1 ( $C_p = 0.42$ ) (see Table 2), the volume flow rate of E2x2\_OR0.5 is 34.5% higher than E2x2\_OR1. This indicates again that the opening ratio, and the resulting internal pressure, is a very important parameter.

The convex roof geometry type is selected to compare the ventilation performance in terms of indoor mean air velocity. Figure 12b to 12e show a comparison of the non-dimensional velocity magnitude ( $|V|/U_{ref}$ ), along four horizontal lines located at a height of  $h = 0.1$  m,  $0.6$  m,  $1.1$  m and  $1.7$  m from the internal floor (as shown in Fig. 12a). Despite the fact that E2x2\_OR1 has the worst performance, locally higher indoor mean velocities are reached than in case E2; e.g. at  $h = 0.6$  m (between  $0.28 < x/D < 0.41$ ) (Fig. 12c), at  $h = 1.1$  m (between  $0.21 < x/D < 0.52$ ) (Fig. 12d) and at  $h = 1.7$  m (between  $0.20 < x/D < 0.65$ ) (Fig. 12e). Figure 12b shows that at  $h = 0.1$  m the reference case (E2) has higher indoor mean velocities over the entire depth of the building compared to the cases E2x2\_OR1 and E2x2\_OR0.5. Figure 12c and 12d show that a double-span roof with opening ratio = 0.5 can increase the indoor mean velocity at  $h = 0.6$  m and  $h = 1.1$  m at the first internal region; i.e. from  $0.20 < x/D < 0.61$  at  $h = 0.6$  m and from  $0 < x/D < 0.73$  at  $h = 1.1$  m.

These results illustrate that the ventilation performance cannot be evaluated based on the volume flow rates only [3]; local effects on the velocity field should be considered as well when assessing the ventilation performance of different building and roof geometries.

## 6 Comparison between all roof geometry types

Figure 13 shows the pressure coefficients in both outlet openings and the volume flow rate through both openings for double-span roof geometries with an opening ratio of 1 ( $OR = 1$ ). It can be seen that for all three roof geometries the  $C_p$  values are larger at the upstream outlet opening (Out.Op.01) than at the downstream opening (Out.Op.02) (Fig. 13a). The largest values at both openings are present for the case with a straight roof geometry (A2x2\_OR1), closely followed by the convex roof geometry (E2x2\_OR1). As a result of the larger pressure coefficients at the first-span outlet opening, the fraction of volume flow rate through this first-span opening is larger than that through the second-span outlet opening. For cases A2x2\_OR1 and E2x2\_OR1, 55.0% of the total volume flow rate exits the building through the first-span outlet opening and 45.0% through the second-span outlet opening. The differences are smaller for case B2x2\_OR1, in which 51.4% of the air is exhausted through the first-span and 48.6% through the second-span opening.

To summarize the results regarding the volume flow rates, Figure 14 shows a comparison of all the single-span and double-span roof geometries analyzed in this study. The convex single-span case E2 reaches the highest volume flow rate within the single-span cases. Therefore, the single-span convex roof geometry E2 is selected as

a reference case (= 100%). The convex double-span E2x2\_OR0.5 reaches the highest volume flow rate from all the cases. The results for all roof geometry cases show that the volume flow rate can be strongly increased by applying opening ratios lower than 1, which is consistent with findings in previous studies on cross-ventilation (e.g. [39]). In addition, it is clear that for straight and concave roof geometries (A2 and B2) the double-span cases perform better than the single span cases.

## 7 Discussion

Based on the volume flow rate and the indoor air velocity in the occupied zone, the current study has evaluated the ventilation performance of single and double-span leeward sawtooth roof configurations for normal wind incidence angle. First, three single-span leeward sawtooth roof geometry types have been evaluated; a straight roof geometry, a concave roof geometry and a convex roof geometry. Then, three double-span leeward sawtooth roof cases with the same three roof geometry types and with the same opening ratio (= 1) as the single-span have been studied. Finally, the same three double-span building geometries, but with smaller opening ratio (= 0.5) have been analyzed.

It is important to mention the limitations of the current study, which should be addressed in future research:

- A successful validation study was presented in this paper for cross-ventilation through a building with asymmetric openings and a flat roof. In the future, it would be very valuable to have experimental data for sawtooth roof buildings to further enhance the validation of the computational model. Preferably, PIV measurements should be conducted to provide flow field data inside and around the building.
- All the single and double-span leeward sawtooth roof geometries have different internal volume as a consequence of the roof geometry; therefore, future research could focus on buildings with the same internal volume in order to eliminate this parameter from the performance evaluation.
- The impact of the wind incidence angle could change the performance of the single and double span leeward sawtooth roof geometry. The study of oblique wind incidence angles will require an additional validation study. For the oblique angles it might be necessary to resort to unsteady simulations, such as Large Eddy Simulations (LES) or Detached Eddy Simulation (DES), to more accurately predict the volume flow rates through the openings resulting from unsteady flow features.
- Surrounding buildings can reduce the airflow rate through naturally ventilated buildings with approximately 30% according to Tominaga and Blocken [58]. In addition, a study by van Hooff and Blocken [33] showed that evaluation of an isolated building (without surrounding buildings) can lead to overestimations of the air change rate per hour (ACH) with up to 96%. Since the surrounding buildings can strongly affect the flow field and thus the natural ventilation flow through a building, this impact should be assessed in the future.
- The present study only considered isothermal wind-induced cross-ventilation, future work should include buoyancy-driven ventilation as well. An assessment of cross-ventilation including buoyancy effects can illustrate the beneficial effects of buoyancy on upward cross-ventilation in leeward sawtooth roof buildings. It will also provide valuable insights for a case in which the wind comes from the other direction (windward sawtooth roof) and wind effects are opposing instead of assisting the buoyancy effects.
- Future research could analyze the influence of the window depth to height ratio. In this study, for the case with an opening ratio of  $OR = 1$ , the depth of the window was about 75% of the height of the window, which might have an effect on the airflow through the window.

## 8 Conclusions

This paper has presented numerical simulations with Computational Fluid Dynamics (CFD) to study the impact of single-span and double-span leeward sawtooth roof geometries on the wind-driven cross-ventilation flow in a generic isolated building. 3D steady RANS simulations with the SST  $k-\omega$  turbulence model have been performed to assess the ventilation performance based on the volume flow rate and the indoor air velocities for normal wind incidence angle. The simulations were based on grid-sensitivity analysis and on validation of the CFD results using Particle Image Velocimetry (PIV) from literature. The following conclusions have been obtained:

- From all the single and double-span geometries with similar opening ratio ( $OR = 1$ ), the convex single-span E2 roof building achieves the highest volume flow rate.
- Within the single-span geometries, the convex single-span E2 results in a 8.8% higher volume flow rate than the concave single-span roof geometry B2, which shows the worst performance with respect to volume flow rate through the building.
- Straight and concave double-span roof geometries result in a slight increase of the volume flow rate compared to single-span roof geometries with similar geometry type. On the other hand, the convex double-span E2x2\_OR1 reaches 12% lower volume flow rate than found for its reference case, the single-span E2.
- For convex double-span cases, such as E2x2\_OR01, the building geometry near the outlet-opening plays an important role in the ventilation performance. The internal geometry contraction near the outlet openings results in higher internal pressure coefficients and reduces the volume flow rate.
- Reducing the opening ratio from 1 to 0.5 for the double-span roof geometries results in an increase of the volume flow rate with 23-39%, depending on the roof geometry.

## Acknowledgments

This work was supported by The National Secretariat of Science, Technology and Innovation (SENACYT) of Panama, and by The Coordination for the Improvement of Higher Level Personnel (CAPES), Brazil, The Civil Construction Engineering Department, Polytechnic School of the University of São Paulo (USP), Brazil and the unit Building Physics and Services of the Department of the Built Environment at Eindhoven University of Technology in the Netherlands.

Twan van Hooff is currently a postdoctoral fellow of the Research Foundation – Flanders (FWO) and is grateful for its financial support (project FWO 12.R9715N).

## References

- [1] Chu C-R, Chiang B-F. Wind-driven cross ventilation in long buildings. *Build Environ* 2014;80:150–8. doi:10.1016/j.buildenv.2014.05.017.
- [2] Montero JI, Hunt GR, Kamaruddin R, Antón A, Bailey BJ. SE—Structures and Environment: Effect of ventilator configuration on wind-driven ventilation in a crop protection structure for the tropics. *J Agric Eng Res* 2001;80:99–107. doi:10.1006/jaer.2000.0694.
- [3] Bartzanas T, Boulard T, Kittas C. Effect of vent arrangement on windward ventilation of a tunnel greenhouse. *Biosyst Eng* 2004;88:479–90. doi:10.1016/j.biosystemseng.2003.10.006.
- [4] Robbins CL. *Daylighting: design and analysis*. Van Nostrand Reinhold Company; 1986.
- [5] Saathoff P, Stathopoulos T. Wind loads on buildings with sawtooth roofs. *J. Struct. Eng.* 1992;118,429–446.
- [6] Stathopoulos T, Saathoff P. Codification of wind pressure coefficients for sawtooth roofs. *J Wind Eng Ind Aerodyn* 1992;43:1727-1738. [http://dx.doi.org/10.1016/0167-6105\(92\)90584-W](http://dx.doi.org/10.1016/0167-6105(92)90584-W).
- [7] Pierre LMS, Kopp GA, Surry D, Ho TCE. The UWO contribution to the NIST aerodynamic database for wind loads on low buildings: Part 2. Comparison of data with wind load provisions. *J Wind Eng Ind Aerodyn* 2005;93:31-59. <http://dx.doi.org/10.1016/j.jweia.2004.07.007>.
- [8] Quan Y, Tamura Y, Matsui M. Mean wind pressure coefficients on surfaces of gable-roofed low-rise buildings. *Adv Struct Eng* 2007;10:259-271. <http://dx.doi.org/10.1260/136943307781422253>.
- [9] Holmes JD. Wind pressures on tropical housing. *J Wind Eng Ind Aerodyn.* 1994;53:105-123. [http://dx.doi.org/10.1016/0167-6105\(94\)90021-3](http://dx.doi.org/10.1016/0167-6105(94)90021-3).
- [10] Holmes JD, Paterson DA. Mean wind pressures on arched-roof buildings by computation. *J Wind Eng Ind Aerodyn* 1993;50:235-242. [http://dx.doi.org/10.1016/0167-6105\(93\)90078-3](http://dx.doi.org/10.1016/0167-6105(93)90078-3).
- [11] Stathopoulos T, Mohammadian AR. Modelling of wind pressures on monoslope roofs. *Eng Struct* 1991;13:281-292. [http://dx.doi.org/10.1016/0141-0296\(91\)90039-F](http://dx.doi.org/10.1016/0141-0296(91)90039-F).
- [12] Cui B. *Wind effects on monosloped and sawtooth roof [PhD thesis]*. Clemson University; 2007.
- [13] Stathopoulos T, Wu H. Knowledge-based wind loading for envelope design: beyond building codes. *J Wind Eng Ind Aerodyn* 1994;53:177-188. [http://dx.doi.org/10.1016/0167-6105\(94\)90025-6](http://dx.doi.org/10.1016/0167-6105(94)90025-6).
- [14] Prasad D, Uliate T, Ahmed MR. Wind loads on low-rise building models with different roof configurations. *Int J Fluid Mech Res* 2009;36:231-243.

- [15] Mistriotis A, Bot GPA, Picuno P, Scarascia-Mugnozza G. Analysis of the efficiency of greenhouse ventilation using computational fluid dynamics. *Agric. For Meteorol* 1997;85:217-28. [http://dx.doi.org/10.1016/S0168-1923\(96\)02400-8](http://dx.doi.org/10.1016/S0168-1923(96)02400-8).
- [16] Mistriotis A, Arcidiacono C, Picuno P, Bot GPA, Scarascia-Mugnozza G. Computational analysis of ventilation in greenhouses at zero- and low-windspeeds. *Agric For Meteorol* 1997;88:121-35. [http://dx.doi.org/10.1016/S0168-1923\(97\)00045-2](http://dx.doi.org/10.1016/S0168-1923(97)00045-2).
- [17] Shklyar A, Arbel A. Numerical model of the three-dimensional isothermal flow patterns and mass fluxes in a pitched-roof greenhouse. *J Wind Eng Ind Aerodyn* 2004;92:1039-59. <http://dx.doi.org/10.1016/j.jweia.2004.05.008>.
- [18] Norton T, Grant J, Fallon R, Sun D-W. Assessing the ventilation effectiveness of naturally ventilated livestock buildings under wind dominated conditions using computational fluid dynamics. *Biosyst Eng* 2009;103:78-99. <http://dx.doi.org/10.1016/j.biosystemseng.2009.02.007>.
- [19] Norton T, Grant J, Fallon R, Sun D-W. Optimising the ventilation configuration of naturally ventilated livestock buildings for improved indoor environmental homogeneity. *Build Environ* 2010;45:983-95. <http://dx.doi.org/10.1016/j.buildenv.2009.10.005>.
- [20] Kobayashi T, Chikamoto T, Osada K. Evaluation of ventilation performance of monitor roof in residential area based on simplified estimation and CFD analysis. *Build Environ* 2013;63:20-30. <http://dx.doi.org/10.1016/j.buildenv.2013.01.018>.
- [21] Gerhardt HJ, Kramer C. Aerodynamic efficiency of smoke ventilators in light streets and shed-type roofs. *J Wind Eng Ind Aerodyn* 1993;45:341-53. [http://dx.doi.org/10.1016/0167-6105\(93\)90105-W](http://dx.doi.org/10.1016/0167-6105(93)90105-W).
- [22] Fatnassi H, Boulard T, Poncet C, Chave M. Optimisation of greenhouse insect screening with computational fluid dynamics. *Biosyst Eng* 2006;93:301-12. <http://dx.doi.org/10.1016/j.biosystemseng.2005.11.014>.
- [23] van Hooff T, Blocken B. Coupled urban wind flow and indoor natural ventilation modelling on a high-resolution grid: a case study for the Amsterdam Arena stadium. *Environ Model Softw* 2010;25:51-65. <http://dx.doi.org/10.1016/j.envsoft.2009.07.008>.
- [24] Gandemer J, Barnaud G. *Ventilation naturelle des habitations sous climat tropical humide: approche aerodynamique*. Nantes: CSTB; 1989.
- [25] Shen X, Zhang G, Bjerg B. Comparison of different methods for estimating ventilation rates through wind driven ventilated buildings. *Energy Build* 2012;54:297–306. doi:10.1016/j.enbuild.2012.07.017.
- [26] Perén JI, van Hooff T, Leite BCC, Blocken B. CFD analysis of cross-ventilation of a generic isolated building with asymmetric opening positions: impact of roof angle and opening location. *Build. Environ* 2015;85:263–76. doi:10.1016/j.buildenv.2014.12.007.
- [27] Perén JI, van Hooff T, Ramponi R, Blocken B, Leite BCC. Impact of roof geometry of an isolated leeward sawtooth-roof building on cross-ventilation: Straight, concave, hybrid or convex? *J Wind Eng Ind Aerodyn* 2015;145:102–14. doi:10.1016/j.jweia.2015.05.014.
- [28] Perén JI, van Hooff T, Leite BCC, Blocken B. Effect of eave configuration in the upward cross-ventilation of a generic isolated leeward sawtooth building: upwind vs leeward eave. *Build. Environ* 2015;92:578–90. doi:10.1016/j.buildenv.2015.05.011.
- [29] Bournet P-E, Boulard T. Effect of ventilator configuration on the distributed climate of greenhouses: A review of experimental and CFD studies. *Comput Electron Agric* 2010;74:195–217. doi:10.1016/j.compag.2010.08.007.
- [30] ISO 7730. *Int. Organ. Stand. Ergon. Therm. Environ. - Anal. Determ. Interpret. Therm. Comf. Using Calc. PMV PPD Indices Local Therm. Comf. Criteria ISO 77302005 Eur. Comm. Stand., Brussels, Belgium: 2005.*
- [31] Ramponi R, Blocken B. CFD simulation of cross-ventilation flow for different isolated building configurations: validation with wind tunnel measurements and analysis of physical and numerical diffusion effects. *J Wind Eng Ind Aerodyn* 2012;104–106: 408–418. <http://dx.doi.org/10.1016/j.jweia.2012.02.005>
- [32] Ramponi R, Blocken B. CFD simulation of cross-ventilation for a generic isolated building: impact of computational parameters. *Build Environ*, 2012;53:34–48. <http://dx.doi.org/10.1016/j.buildenv.2012.01.004>
- [33] van Hooff T, Blocken B. On the effect of wind direction and urban surroundings on natural ventilation of a large semi-enclosed stadium. *Comput Fluids* 2010;39:1146–1155. <http://dx.doi.org/10.1016/j.compfluid.2010.02.004>
- [34] van Hooff T, Blocken B. CFD evaluation of natural ventilation of indoor environments by the concentration decay method: CO<sub>2</sub> gas dispersion from a semi-enclosed stadium. *Build Environ* 2013;61:1–17 <http://dx.doi.org/10.1016/j.buildenv.2012.11.021>
- [35] Kato S, Murakami S, Mochida A, Akabayashi S, Tominaga Y. Velocity-pressure field of cross ventilation with open windows analyzed by wind tunnel and numerical simulation. *J Wind Eng Ind Aerodyn* 1992;44: 2575–2586. [http://dx.doi.org/10.1016/0167-6105\(92\)90049-G](http://dx.doi.org/10.1016/0167-6105(92)90049-G)

- [36] Jiang Y, Alexander D, Jenkins H, Arthur R, Chen Q. Natural ventilation in buildings: measurement in a wind tunnel and numerical simulation with large-eddy simulation. *J Wind Eng Ind Aerodyn* 2003;91:331–353. [http://dx.doi.org/10.1016/S0167-6105\(02\)00380-X](http://dx.doi.org/10.1016/S0167-6105(02)00380-X).
- [37] Blocken B. 50 years of Computational Wind Engineering: Past, present and future. *J Wind Eng Ind Aerodyn* 2014;129: 69-102.
- [38] Wolfram MathWorld. n.d. <http://mathworld.wolfram.com/ConvexFunction.html> (accessed December 1, 2014).
- [39] Karava P, Stathopoulos T, Athienitis AK. Airflow assessment in cross-ventilated buildings with operable façade elements. *Build Environ* 2011;46:266–79. doi:10.1016/j.buildenv.2010.07.022.
- [40] Franke J, Hellsten A, Schlunzen KH, Carissimo B. Best Practice Guideline for CFD simulation of flows in the urban environment. Bruss COST 2007. doi:10.1504/IJEP.2011.038443.
- [41] Tominaga Y, Mochida A, Yoshie R, Kataoka H, Nozu T, Yoshikawa M, et al. AIJ guidelines for practical applications of CFD to pedestrian wind environment around buildings. *J Wind Eng Ind Aerodyn* 2008;96:1749–61. doi:16/j.jweia.2008.02.058.
- [42] Blocken B. Computational Fluid Dynamics for urban physics: Importance, scales, possibilities, limitations and ten tips and tricks towards accurate and reliable simulations. *Build. Environ* 2015;91:219–45. doi:10.1016/j.buildenv.2015.02.015.
- [43] Karava P. Airflow prediction in buildings for natural ventilation design: wind tunnel measurements and simulation. Department of Building, Civil and Environmental Engineering, Concordia University, 2008.
- [44] Blocken B, Stathopoulos T, Carmeliet J. CFD simulation of the atmospheric boundary layer: wall function problems. *Atmos Environ* 2007;41:238–52. doi:16/j.atmosenv.2006.08.019.
- [45] Blocken B, Carmeliet J, Stathopoulos T. CFD evaluation of wind speed conditions in passages between parallel buildings—effect of wall-function roughness modifications for the atmospheric boundary layer flow. *J Wind Eng Ind Aerodyn* 2007;95:941–62. doi:10.1016/j.jweia.2007.01.013.
- [46] ANSYS. *Fluent 12 user's guide*. Lebanon: Fluent Inc. 2009.
- [47] Menter FR. Two-equation eddy-viscosity turbulence models for engineering applications. *AIAA J* 1994;32:1598–605.
- [48] Launder BE, Spalding DB. *Lectures in mathematical models of turbulence*. Academic Press, London, England, 1972.
- [49] Shih TH, Liou WW, Shabbir A, Yang Z, Zhu J. A new k-ε eddy viscosity model for high Reynolds number turbulent flows. *Comput Fluids* 1995;24:227–38.
- [50] Yakhot V, Orszag SA, Thangam S, Gatski TB, Speziale CG. Development of turbulence models for shear flows by a double expansion technique. *Phys Fluids Fluid Dyn* 1992;4:1510–20.
- [51] Choudhury D. *Introduction to the renormalization group method and turbulence modeling*. 1993.
- [52] Wilcox DC. *Turbulence modeling for CFD*. California: DCW Industries, Inc.; 1993.
- [53] Launder BE, Reece GJ, Rodi W. Progress in the development of a Reynolds-stress turbulence closure. *J Fluid Mech* 1975;68:537–66. doi:10.1017/S0022112075001814.
- [54] Wieringa J. Updating the Davenport roughness classification. *J Wind Eng Ind Aerodyn* 1992;41:357–68. doi:10.1016/0167-6105(92)90434-C.
- [55] Launder BE, Spalding DB. The numerical computation of turbulent flows. *Comput Methods Appl Mech Eng* 1974;3:269–89. doi:10.1016/0045-7825(74)90029-2.
- [56] Cebeci T, Bradshaw P. *Momentum transfer in boundary layers*. Hemisphere Publishing Corp. New York: 1977.
- [57] ISO 2533. International Organization for Standardization. *Standard Atmosphere*. International Standards Organization; 1975.
- [58] Tominaga Y, Blocken B. Wind tunnel experiments on cross-ventilation flow of a generic building with contaminant dispersion in unsheltered and sheltered conditions. *Build Environ* 2015;92:452–61. doi:10.1016/j.buildenv.2015.05.026.

## TABLES

Table 1. Internal volume ( $m^3$ ) of the building with different single and double-span roof geometries.

Building case name	Volume ( $m^3$ )
Single-span	
A2	118.63
B2	129.63
E2	112.14
Double-span	
A2x2	119.00
B2x2	131.04
E2x2	108.70

Table 2. Area-averaged pressure coefficient ( $C_p$ ) at both the inlet and the outlet opening(s) of both the single-span and the double-span leeward sawtooth roof geometry cases.

Building case name	Pressure coefficient ( $C_p$ )		
	Inlet opening	Outlet opening	
A2	0.38	-0.25	
B2	0.40	-0.24	
E2	0.37	-0.28	
		Out. Op. 1	Out. Op 2
A2x2_OR1	0.37	-0.36	-0.18
B2x2_OR1	0.40	-0.21	-0.14
E2x2_OR1	0.42	-0.33	-0.14
A2x2_OR05	0.25	-0.31	-0.17
B2x2_OR05	0.29	-0.18	-0.13
E2x2_OR05	0.25	-0.32	-0.14

FIGURES

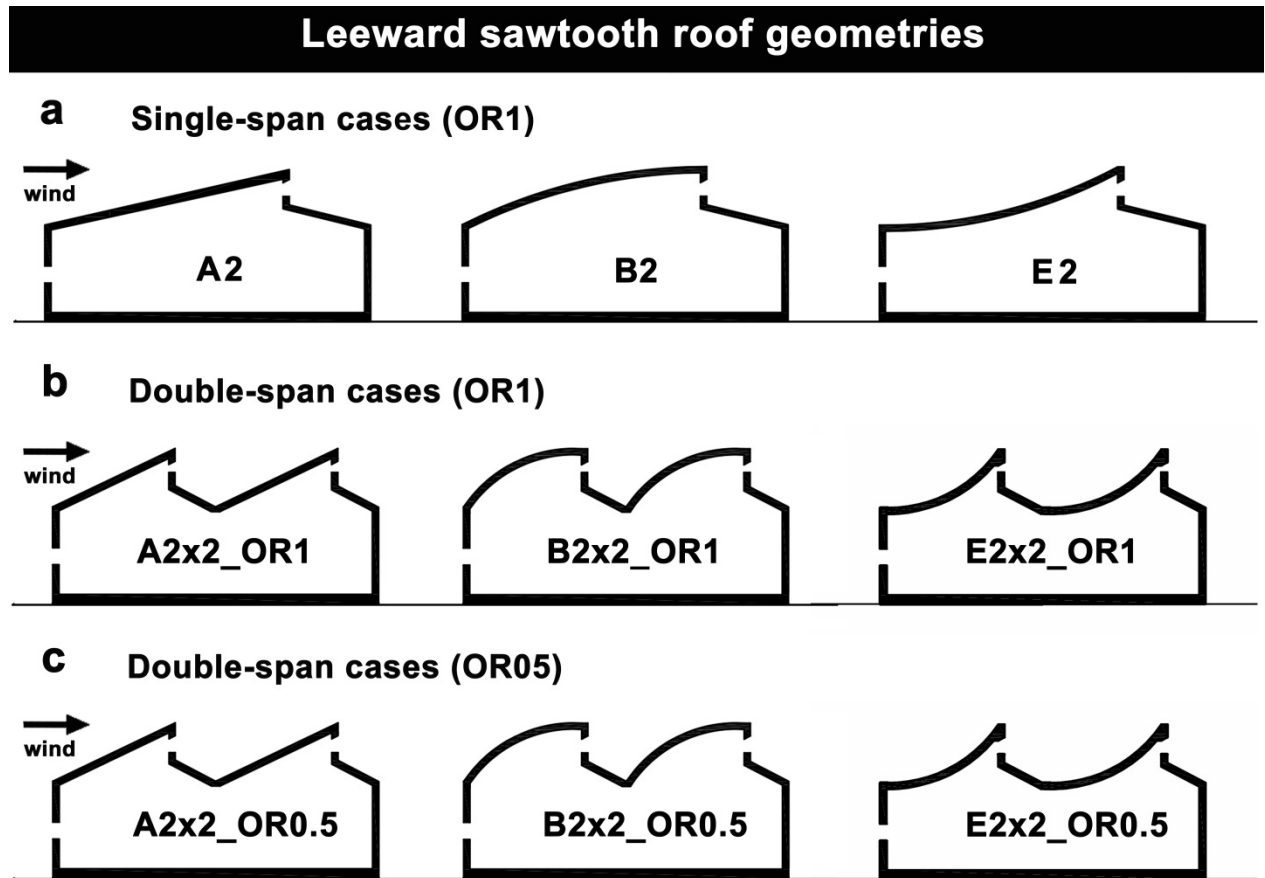


Figure 1: Longitudinal cross-section of the leeward sawtooth roof cases analyzed. (a) Single-span leeward sawtooth roof buildings: A2 (straight roof), B2 (concave roof) and E2 (convex roof); (b) double-span cases with opening ratio (OR) equal to that of the single-span cases ( $OR = 1$ ): A2x2\_OR1, B2x2\_OR1 and E2x2\_OR1; (c) double-span cases with lower opening ratio than single-span cases ( $OR = 0.5$ ): A2x2\_OR0.5, B2x2\_OR0.5 and E2x2\_OR0.5.

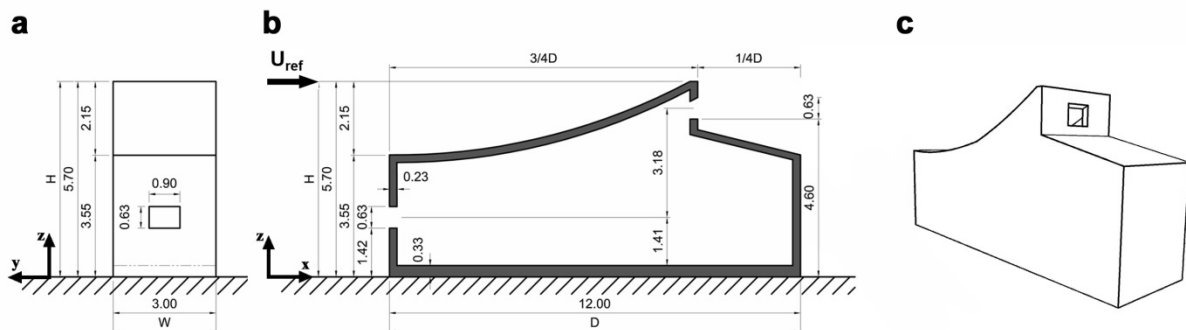


Figure 2: Overview of dimensions of case E2 (dimensions in m). (a) Front view (upwind facade) with opening size and dimensions. (b) Vertical cross-section with opening size and dimensions. (c) Perspective view. The other roof geometries (A,B) have the same roof height, facade porosity (inlet-outlet opening size), building depth (D) and width (W); however, they have different roof geometries and consequently different internal volumes.

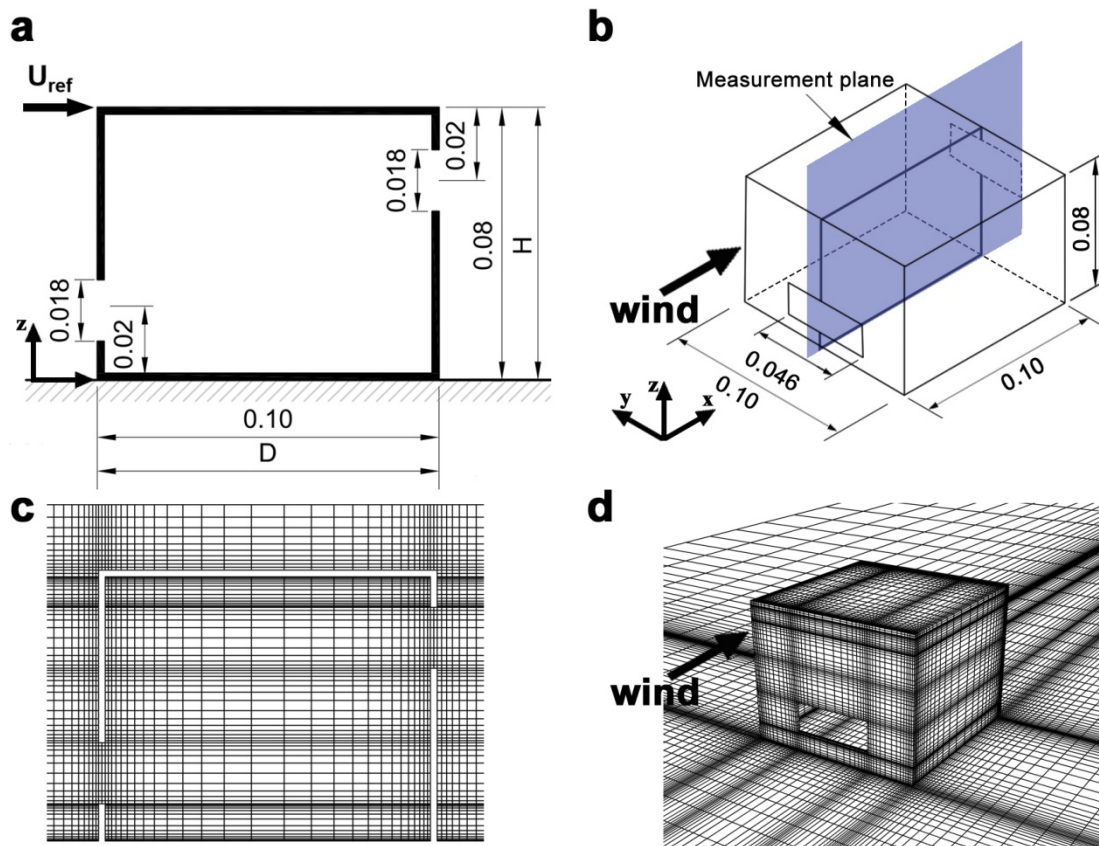


Figure 3: (a) Vertical cross-section of the reduced-scaled building model as studied by Karava et al. [39] with opening size and dimensions (in meter). (b) Perspective view with measurement plane and dimensions (in meter). (c) Computational grid in building vertical center plane (770,540 cells). (d) Perspective view of grid on the building surfaces and part of ground surface.

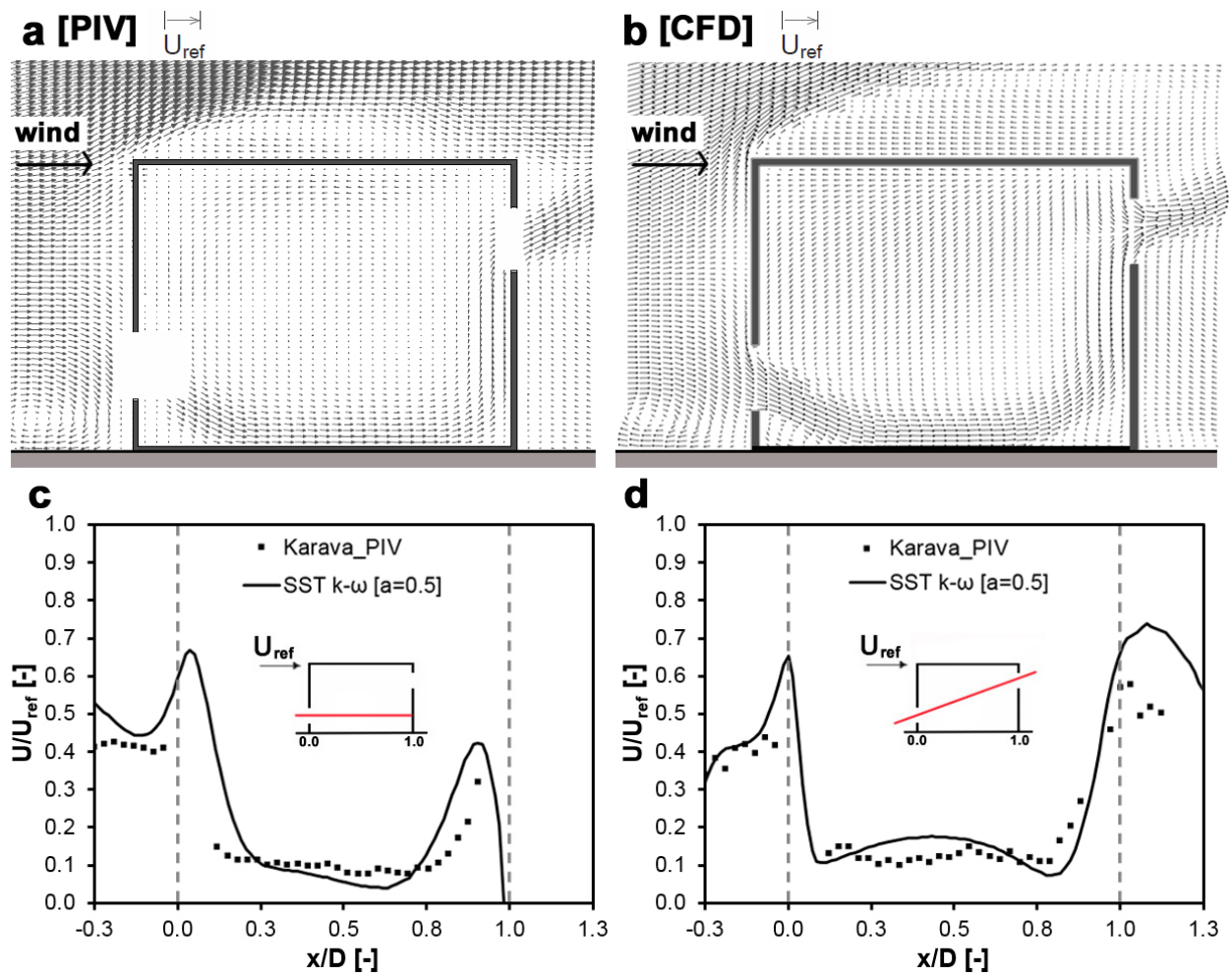


Figure 4: (a, b) Comparison of the mean velocity in the vertical center plane obtained from: (a) PIV measurements (processed from [39]); and (b) CFD simulation. (c,d) Streamwise wind speed ratio  $U/U_{ref}$  from PIV measurements and CFD simulation along: (c) horizontal line; and (d) diagonal line [26].

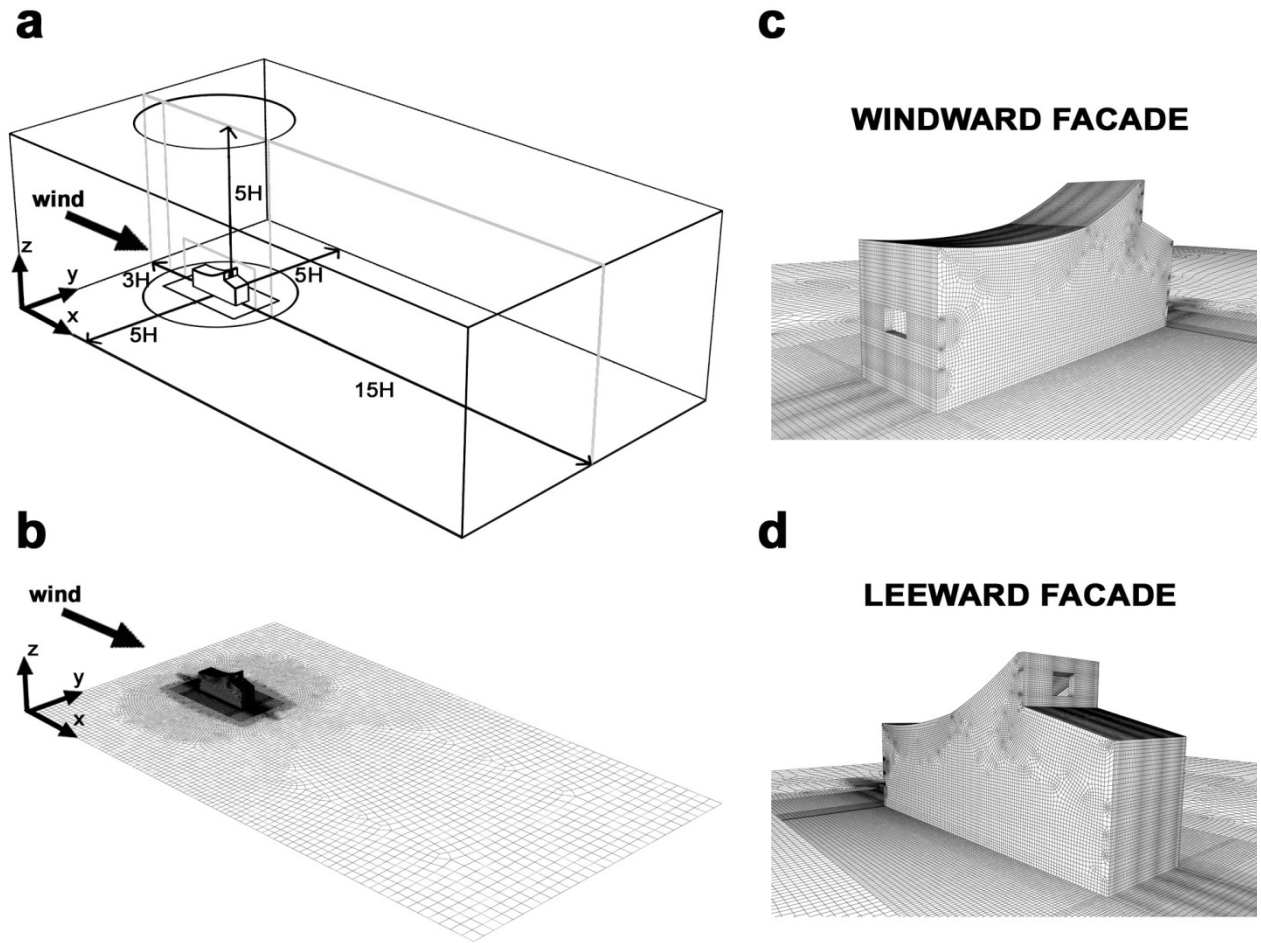


Figure 5: (a) Perspective view of building case E2 in its computational domain. (b-d) Perspective view of the computational grid for building case E2 (total number of cells: 2,917,152). (b) View of the computational grid on building surfaces and ground surface. (c) Close-up view of the windward facade (inlet opening). (d) Close-up view of the leeward facade (outlet opening).

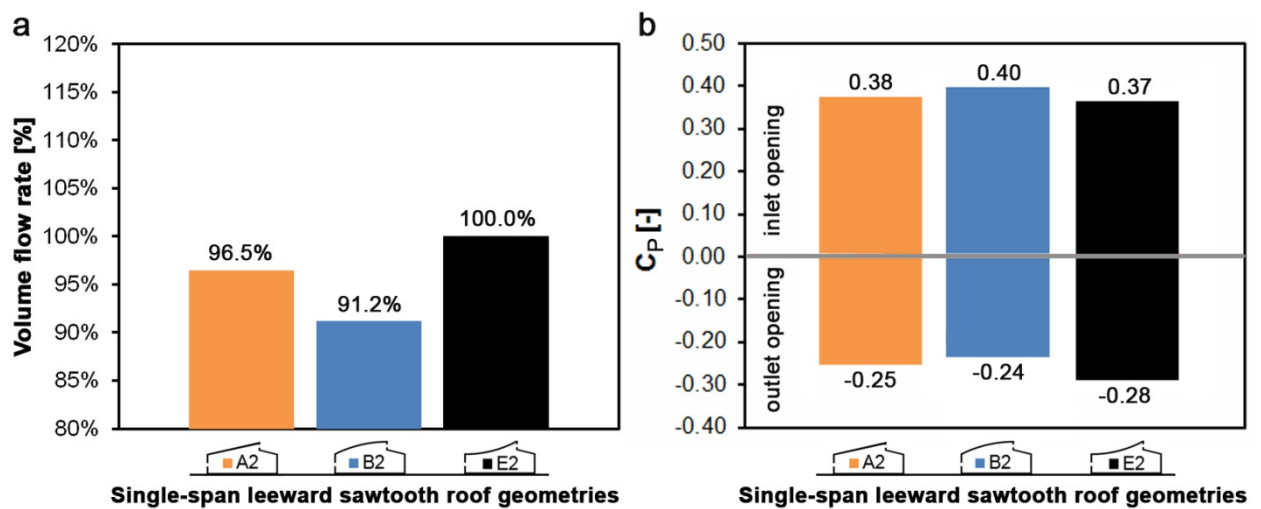


Figure 6: Impact of roof geometry for single-span cases. (a) Volume flow rate through the building. (b) Area-averaged pressure coefficient ( $C_p$ ) in the outlet opening surface under normal wind incidence angle.

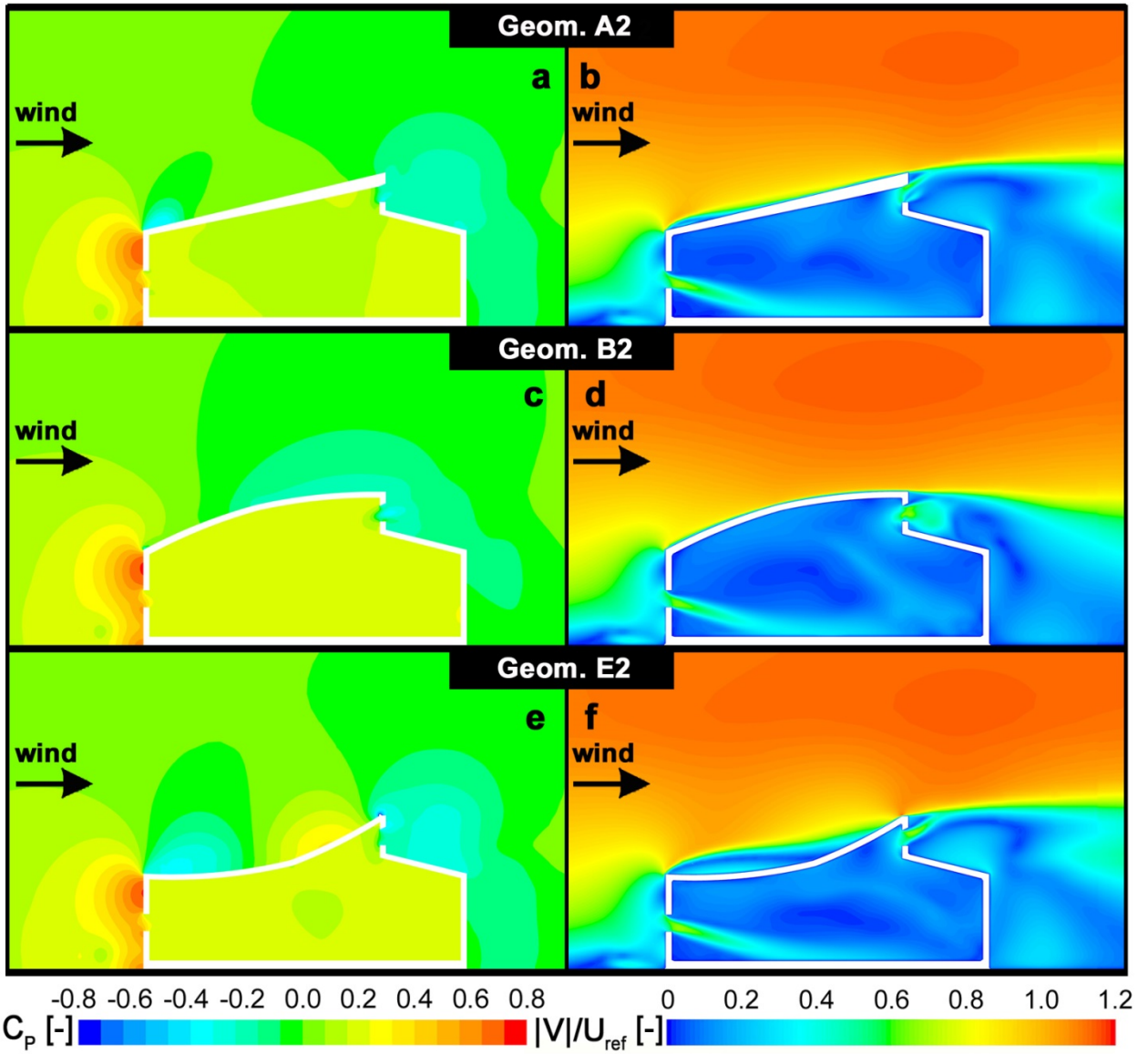


Figure 7: Contour plots of pressure coefficient  $C_p$  (a,c,e) and non-dimensional velocity magnitude ( $|V|/U_{ref}$ ) (b,d,f) in the vertical center plane for the three single-span leeward sawtooth roof geometries. (a,b) Straight roof A2. (c,d) Concave roof B2. (e,f) Convex roof E2.

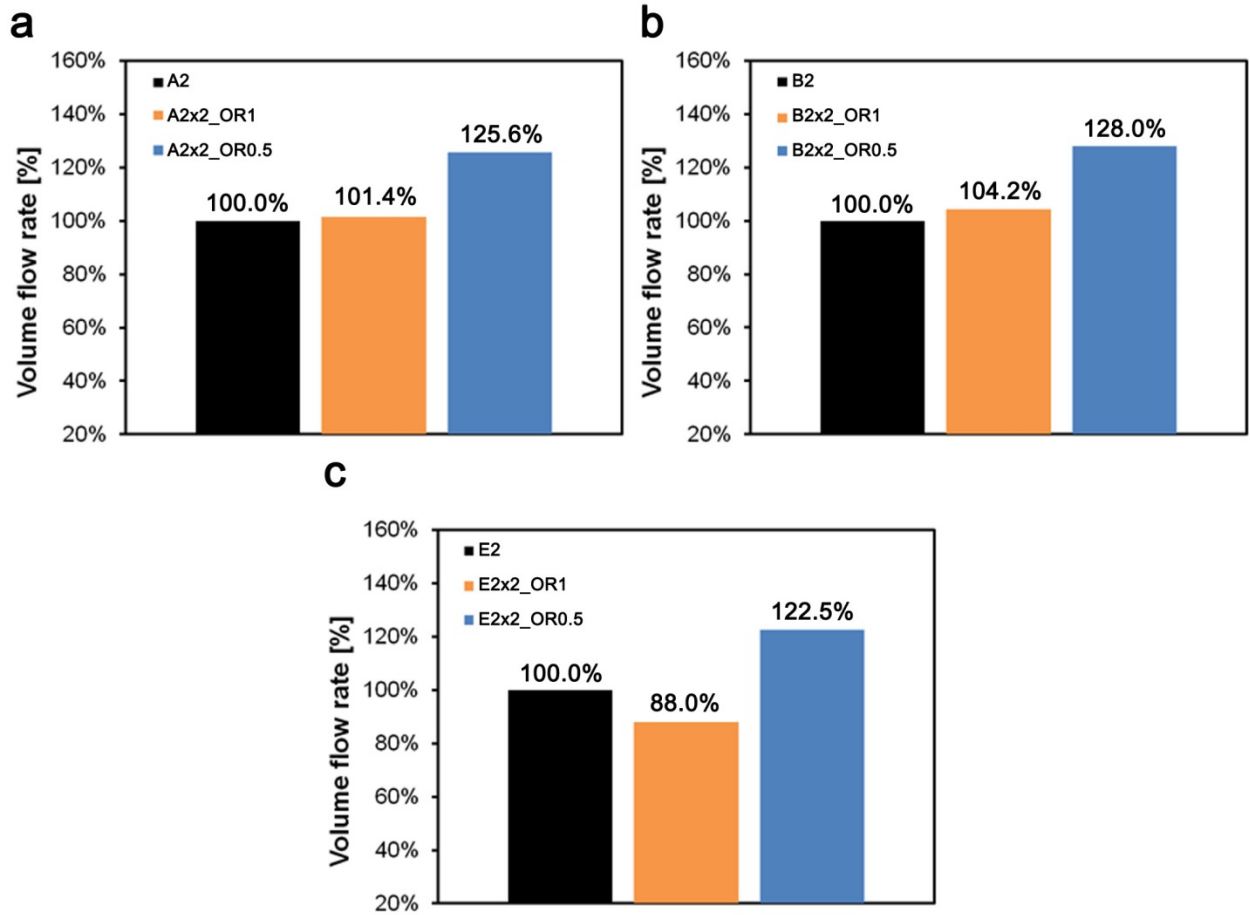


Figure 8: Impact of roof geometry and opening ratio on the volume flow rate under normal wind incidence angle for single-span and double-span leeward sawtooth roof geometries. (a) Straight roof case A2, A2x2\_OR1 and A2x2\_OR0.5. (b) Concave roof case B2, B2x2\_OR1 and B2x2\_OR0.5. (c) Convex roof case E2, E2x2\_OR1 and E2x2\_OR0.5.

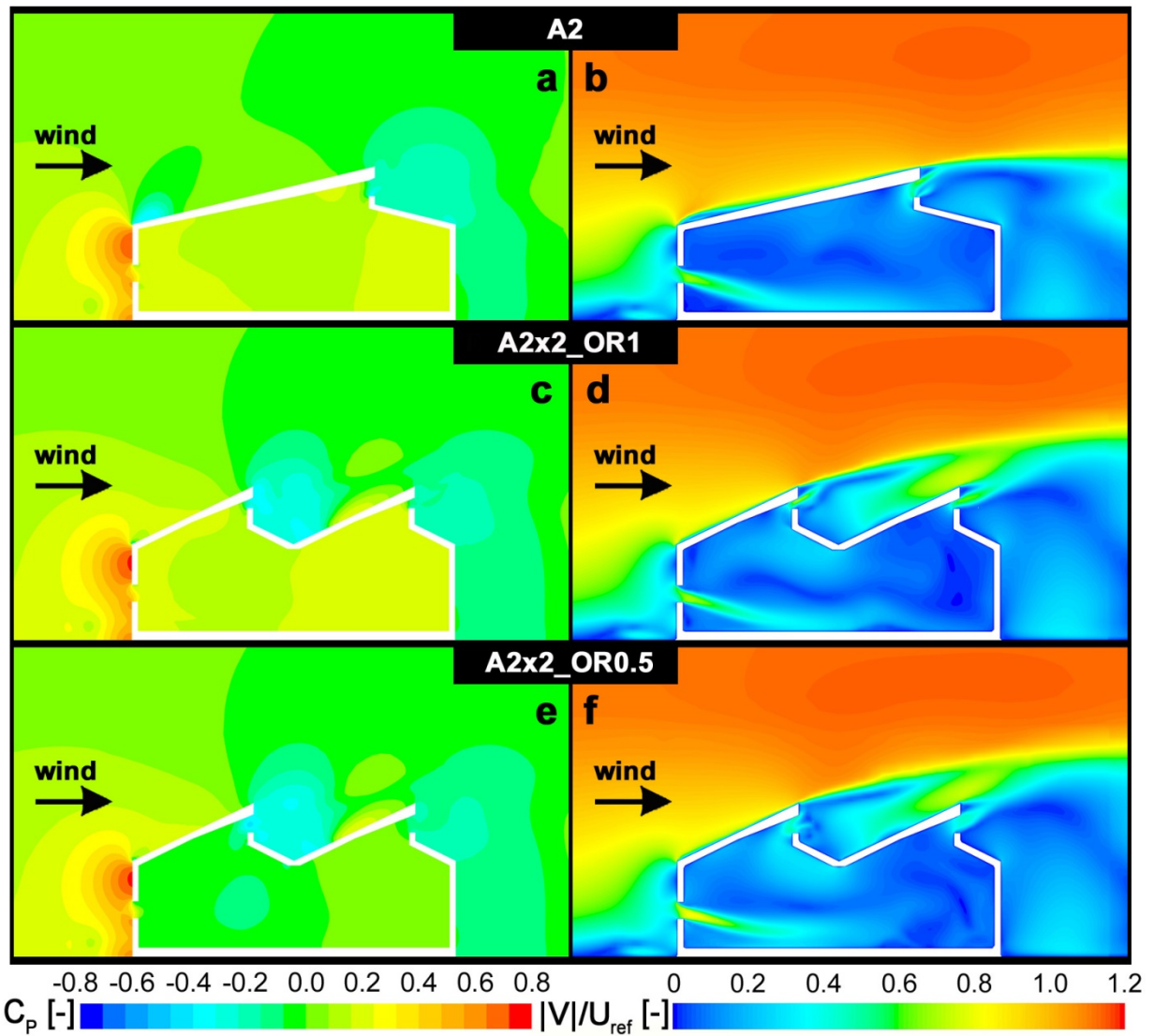


Figure 9: Contour plots of pressure coefficient  $C_p$  (a,c,e) and non-dimensional velocity magnitude ( $|V|/U_{ref}$ ) (b,d,f) in the vertical center plane for the three cases with a straight roof geometry: (a,b) Single-span geometry A2. (c,d) Double-span geometry A2x2\_OR1. (e,f) Double-span geometry A2x2\_OR0.5.

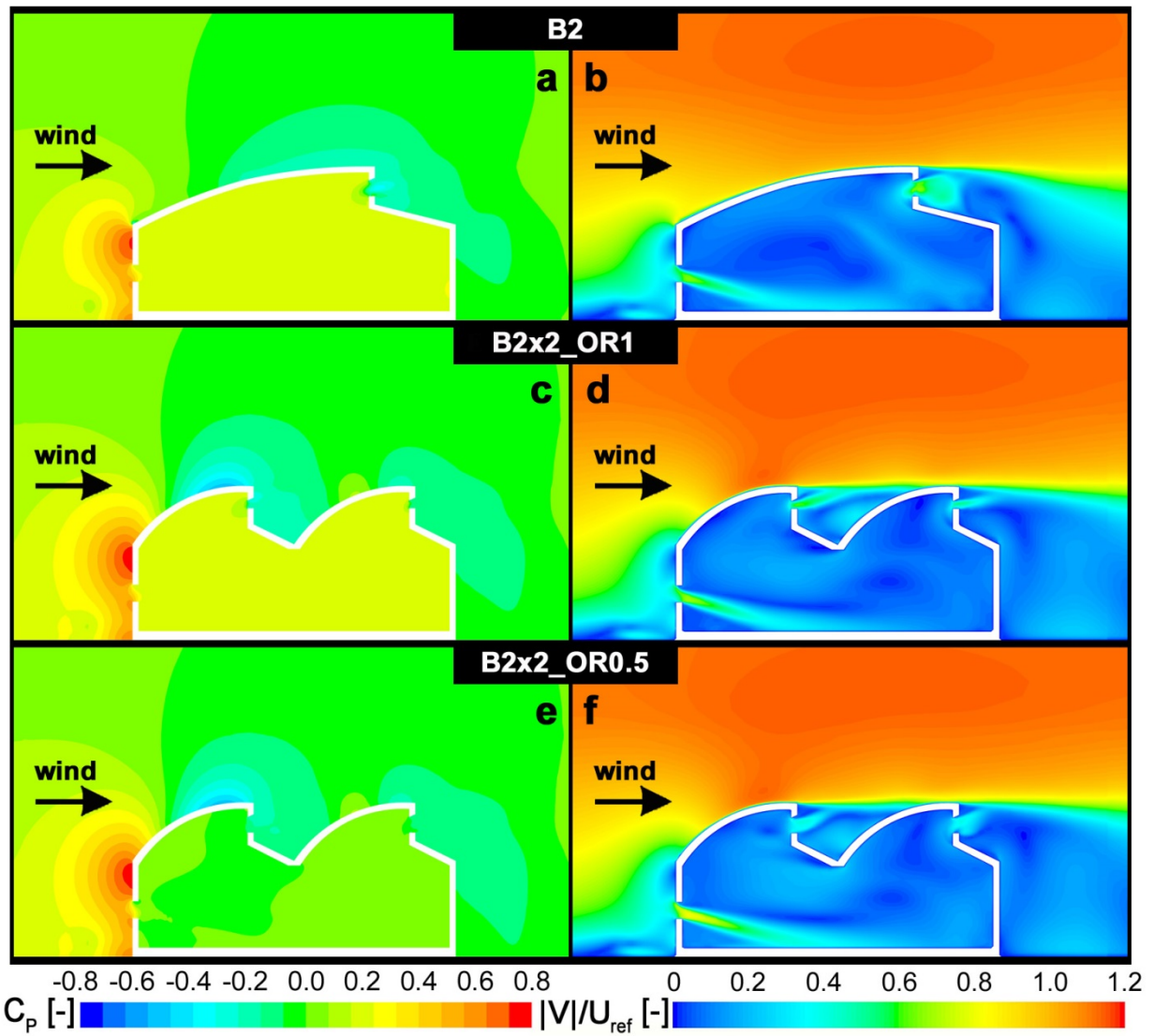


Figure 10: Contour plots of pressure coefficient  $C_p$  (a,c,e) and non-dimensional velocity magnitude ( $|V|/U_{ref}$ ) (b,d,f) in the vertical center plane for the three cases with a concave roof geometry: (a,b) Single-span geometry B2. (c,d) Double-span geometry B2x2\_OR1. (e,f) Double-span geometry B2x2\_OR0.5.

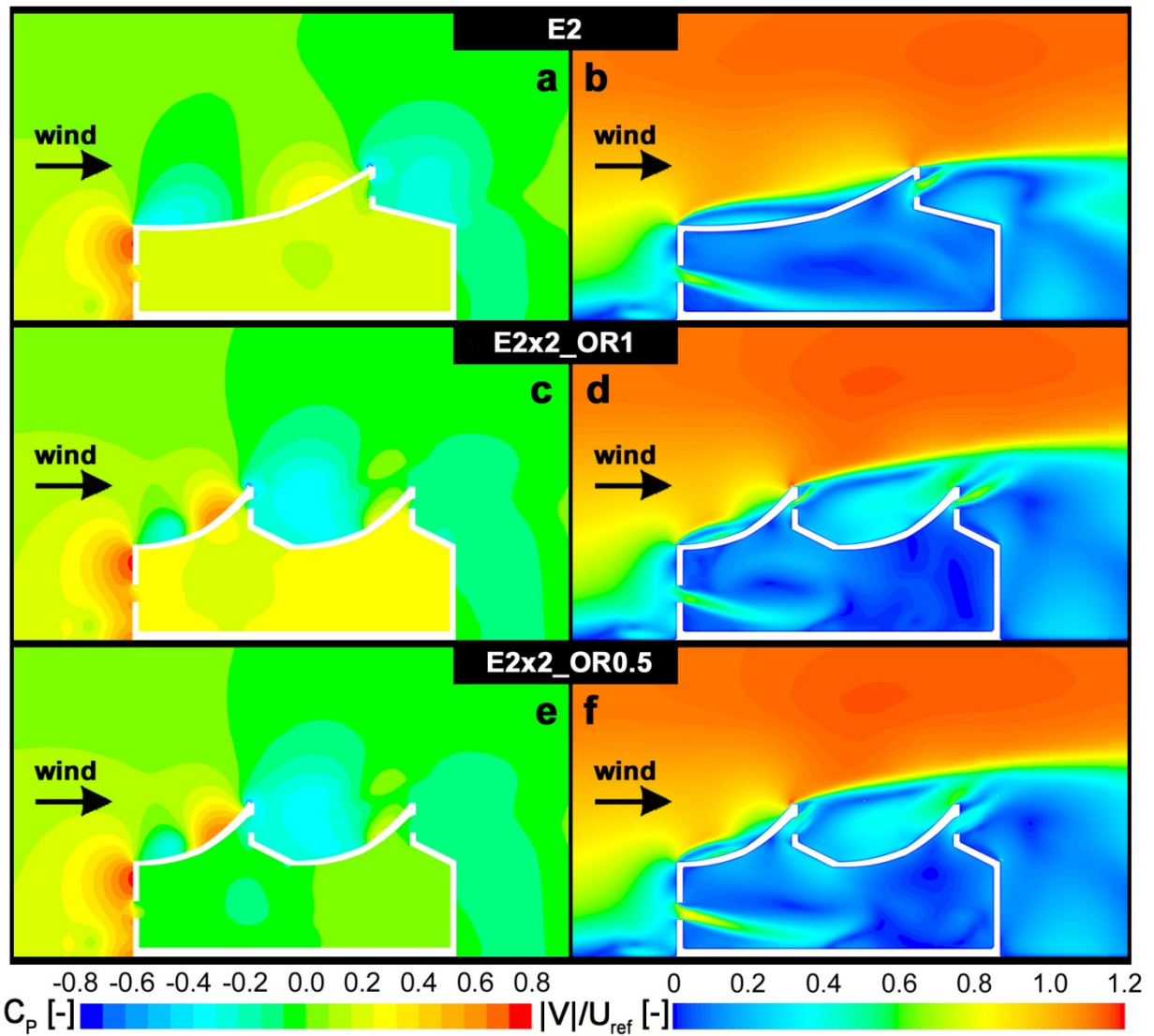


Figure 11: Contour plots of pressure coefficient  $C_p$  (a,c,e) and non-dimensional velocity magnitude ( $|V|/U_{ref}$ ) (b,d,f) in the vertical center plane for the three cases with a convex roof geometry. (a,b) Single-span geometry E2. (c,d) Double-span geometry E2x2\_OR1. (e,f) Double-span geometry E2x2\_OR0.5. The dashed circles in (c,d) indicate the narrow outlet openings.

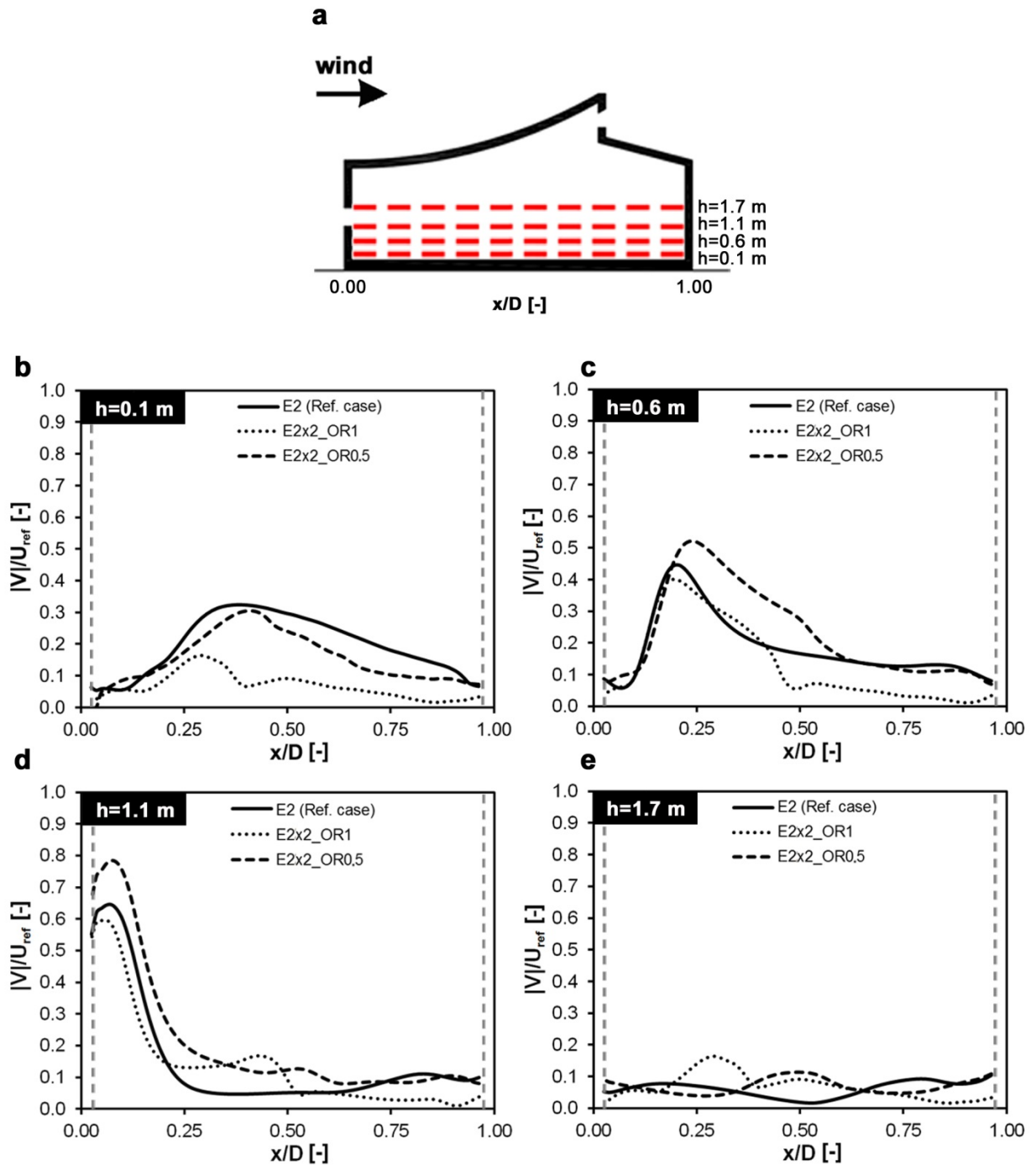


Figure 12: Impact of the roof geometry and opening ratio on the non-dimensional velocity magnitude ( $|V|/U_{ref}$ ) under a normal wind incidence angle for convex roof cases E2, E2x2\_OR1 and E2x2\_OR0.5 along four horizontal lines at a height  $h$  above the floor. (a) Geometry E2 with indication of the four horizontal lines. (b-e) Results at (b)  $h = 0.1$  m. (c)  $h = 0.6$  m. (d)  $h = 1.1$  m. (e)  $h = 1.7$  m. The dashed vertical lines indicate the inner surfaces of the walls at the windward and leeward side of the building.

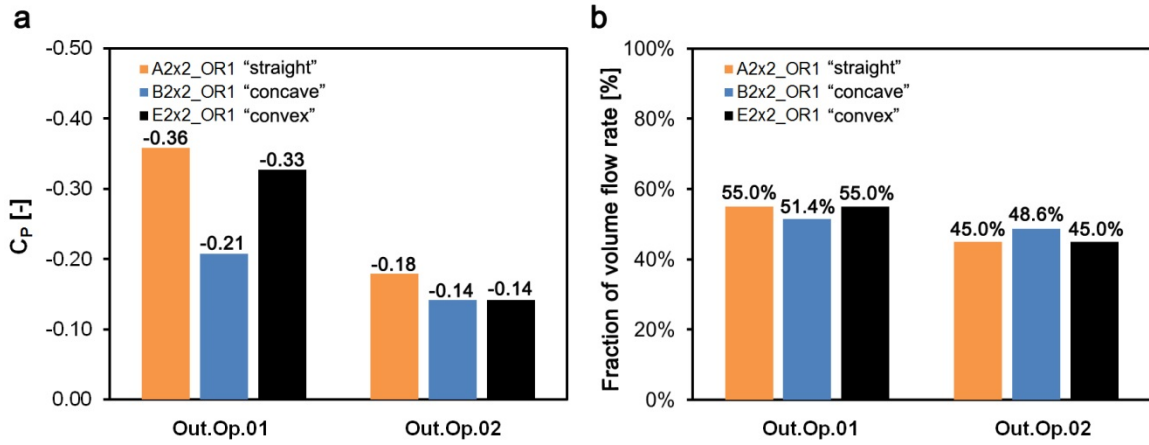


Figure 13: Impact of the roof geometry (straight, concave, convex) (opening ratio = 1). (a) Pressure coefficient ( $C_p$ ) in outlet opening 1 (Out.Op.01) and outlet opening 2 (Out.Op.02). (b) Fraction of volume flow rate through outlet openings 1 and 2.

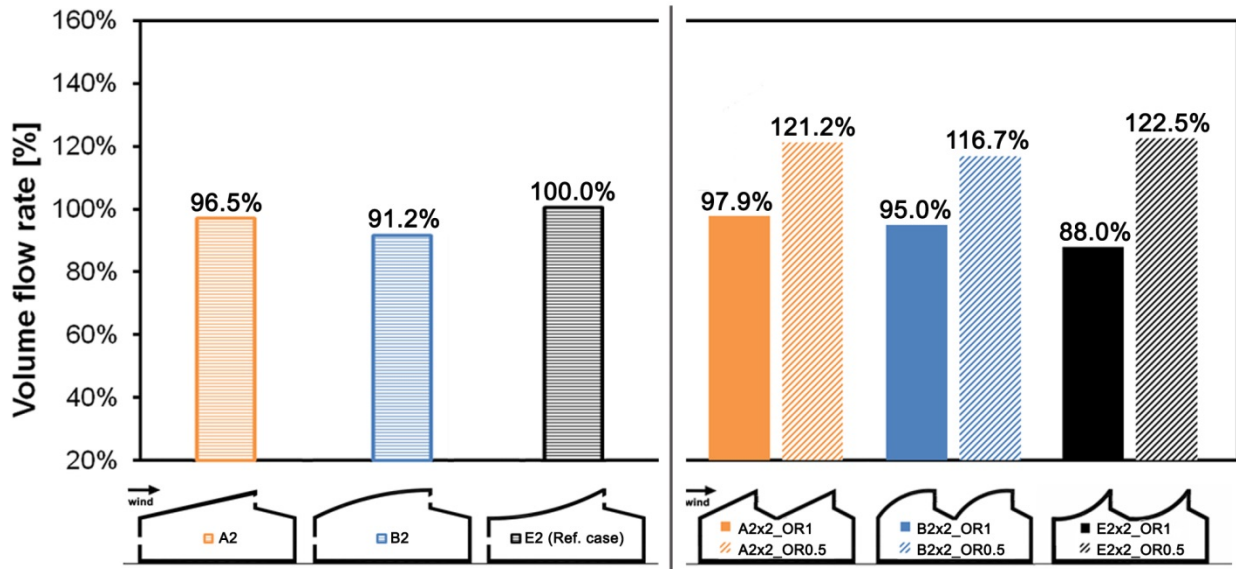


Figure 14: Impact of roof geometry and opening ratio for the three single-span roof geometries (A2, B2, E2) and six double-span leeward sawtooth roof geometries on the volume flow rate. The single-span geometry E2 is taken as reference case (= 100%).